Chapter V

Time-Resolved Electron Paramagnetic Resonance Spectroscopy on HDPP-Pent, Li_2(DPP-Pent)$_2$, and KDPP-Pent

Introduction

Singlet fission is a multiexciton generating process by which two triplets may be generated from one singlet exciton.[1] This process proceeds through a correlated triplet pair state ^{M}(TT). Although the singlet character of the ^{M}(TT) state provides a spin-allowed pathway between singlet and triplet manifolds, the coupling of two triplets gives rise to nine states of different spin multiplicities.[2–4] In the high-field limit, these sublevels will approach the eigenstates of the $\hat{S}^2$ and $\hat{S}_z$ operators and represent states of singlet, triplet, and quintet multiplicity. Recent reports using time-resolved electron paramagnetic resonance (TREPR) spectroscopy have elucidated the formation of quintet states via singlet fission in material and molecular systems. The features of these TREPR spectra often suggest that the quintet is generated in a strongly exchange coupled triplet pair (J >> D), such that the eigenstates are roughly of pure spin multiplicity.[5–13]

The triplet pair states play a vital role in the singlet fission conversion process from singlet to free triplets that might be harvested in a solar energy device. Additionally, recent interest has been given to the triplet pair state for quantum information science because the triplet pair represents a maximally entangled state.[5,14,15] Ideally, in quantum information science, one can initialize the system with a high degree of polarization, which is possible for the triplet pair states. Recent investigations have demonstrated that the spin polarization of the quintet observed by TREPR is highly dependent on the relative orientation of the chromophores and their relative orientation with the applied magnetic field. Strict alignment of the molecular axes with each other and with the field produces maximal spin polarization, largely in the $M_s = 0$ sublevel.[15]

As this example shows, it is critically important to be able to understand the structural and electronic properties of singlet fission systems that give rise to different properties of the triplet pair states if we are to rationally design and apply them. To that end, molecular bipentacenes can

be very useful to study and compare with respect to their TREPR data to trace polarization and time evolution of the quintet triplet pair states and uncorrelated triplet features. In this chapter we present results and preliminary analysis regarding the TREPR spectra collected on HDPP-Pent, Li_2(DPP-Pent)$_2$, and KDPP-Pent. Appendix C contains the theoretical framework in the construction of triplet pair spin operators and spin Hamiltonians.

Time-Resolved EPR Spectroscopy

In time-resolved EPR (TREPR), a laser flash is applied to the sample and an EPR signal can be collected at certain time delays after the flash (DAFs). As a result, high-spin excited states may be probe by EPR even if the system is diamagnetic in its ground state. TREPR can be done in continuous wave (CW) mode or in pulsed mode. In CW mode, the laser flash is applied to the sample while the microwave radiation is continuously applied to the cavity, and the EPR spectrum can be read at a particular time by sweeping the magnetic field. This mode of collection has certain drawbacks, as the continuously applied microwave field can induce spin relaxation within the sample, decreasing the lifetime of the signal. In pulsed mode, the EPR signal intensity at a given time after the laser flash is read out by a Hahn echo sequence.

The pulsed detection has certain advantages over the CW detection scheme. As the microwave radiation is not applied continuously, the pulsed detection reduces microwave-driven spin relaxation. Additionally, pulsed detection makes possible the selective detection of transitions arising from specific spin states. The Hahn echo sequence reads out the net magnetization in the transverse plane of the rotating reference frame. The magnetic moments of the spin, initially aligned with the externally applied field along the z-axis, are rotated into the transverse plane by the pulsed application of the $\boldsymbol{B_1}$ field. As the magnetic moment of a spin system is proportional to its total spin angular momentum, systems with higher total spin angular momentum S will

generally exhibit greater magnitude magnetic moments μ. The perpendicularly applied $\boldsymbol{B_1}$ field imposes a torque on the magnetic moment of the spin system. The greater the magnitude of the magnetic moment of the spin system, the greater the torque and thus the greater the angular velocity with which the magnetic moment rotates. As such, the Rabi nutation frequency of a given spin packet will be dependent on the spin angular momentum quantum number S and the magnetic sublevel quantum number M_s. This is given in the expression below in which $\Omega_{M_s,M_s\pm1}$ represents the nutation frequency of a given spin packet and ω_1 is the $\boldsymbol{B_1}$ magnetic field strength in angular frequency units.[16]

$$\Omega_{M_s,M_s\pm1} = \omega_1\sqrt{S(S+1) - M_s(M_s \pm 1)} \qquad Eq.\,5.1$$

In standard EPR spectroscopy, the spin sublevels follow a Boltzmann distribution of the populations. As such, the population of the lower energy sublevel of a given transition (P_l) is greater than the population of the upper energy sublevel (P_u), which results in a net absorptive signal for each transition. In TREPR, the laser flash generates a nonequilibrium population distribution among the spin states. As a result, TREPR spectra can feature both net absorptive and net emissive signals.

As written out explicitly in Appendix C, we derive the spin Hamiltonian for the triplet pair state from the individual triplet spin operators. We follow in the vein of past triplet pair descriptions including recent work such as the JDE model.[14,17] We consider only intratriplet dipolar interactions and intertriplet exchange when including the zero-field splitting and exchange Hamiltonians, respectively. We include only the isotropic component of the exchange as this is generally the dominant exchange interaction in molecular organic electron spin systems.[18] This gives a spin Hamiltonian $\hat{H}$ of the form below:

$$\hat{H} = \hat{H}_{zee} + \hat{H}_{zfs} + \hat{H}_{ex}$$

$$\hat{H}_{zee} = \hat{H}^{A}_{zee} \otimes I_3 + I_3 \otimes \hat{H}^{B}_{zee}$$

$$\hat{H}^{A,B}_{zee} = \mu_B \boldsymbol{B^T} \cdot \boldsymbol{g^{A,B}} \cdot \boldsymbol{S^{A,B}}$$

$$\hat{H}_{zfs} = \hat{H}^{A}_{zfs} \otimes I_3 + I_3 \otimes \hat{H}^{B}_{zfs}$$

$$\hat{H}^{A,B}_{zfs} = \boldsymbol{S^{A,B^T}} \cdot \boldsymbol{D^{A,B}} \cdot \boldsymbol{S^{A,B}}$$

$$\hat{H}_{ex} = J(\hat{S}^{A}_{x} \otimes \hat{S}^{B}_{x} + \hat{S}^{A}_{y} \otimes \hat{S}^{B}_{y} + \hat{S}^{A}_{z} \otimes \hat{S}^{B}_{z}) \qquad Eq. 5.2A - F$$

$\hat{H}^{A,B}_{zee}$ and $\hat{H}^{A,B}_{zfs}$ represent the Zeeman and zero-field splitting Hamiltonians for individual triplets A or B and $\hat{H}_{ex}$ represents the exchange interaction between triplets A and B.[9,14,17,19–21]

In collaboration with Drs. Jens Niklas and Oleg Poluektov, we collected TREPR data on Li_2(DPP-Pent)$_2$, HDPP-Pent, and KDPP-Pent. The compounds were synthesized at Caltech. The data collection was performed at Argonne National Laboratory. EPR simulations were run using the EasySpin package developed for MATLAB.[22] Simulation of the ^{5}(TT) spectra using polarization in the spin basis was performed using an additional script for EasySpin developed by Dr. Matthew Krzyaniak.

Results

Li_2(DPP-Pent)$_2$

TREPR data was collected on 2 mM frozen glass solution samples of Li_2(DPP-Pent)$_2$. We collected EDFS spectra at microwave power attenuations of 17 and 12 dB to measure quintet- and triplet-selective spectra, respectively shown in Figure 5.1. As can be seen, the EDFS spectra collected at 17 dB, although predominately featuring quintet transitions, does have some intensity

coming from triplet transitions on the wings. The absolute signal intensity rises going from 300 ns to 5 μs and then is largely decayed by 70 μs. When normalized, the spectral features at 300 ns and 5 μs are consistent with each other. However, by 70 μs, the quintet features have largely decayed while the triplet features persist.

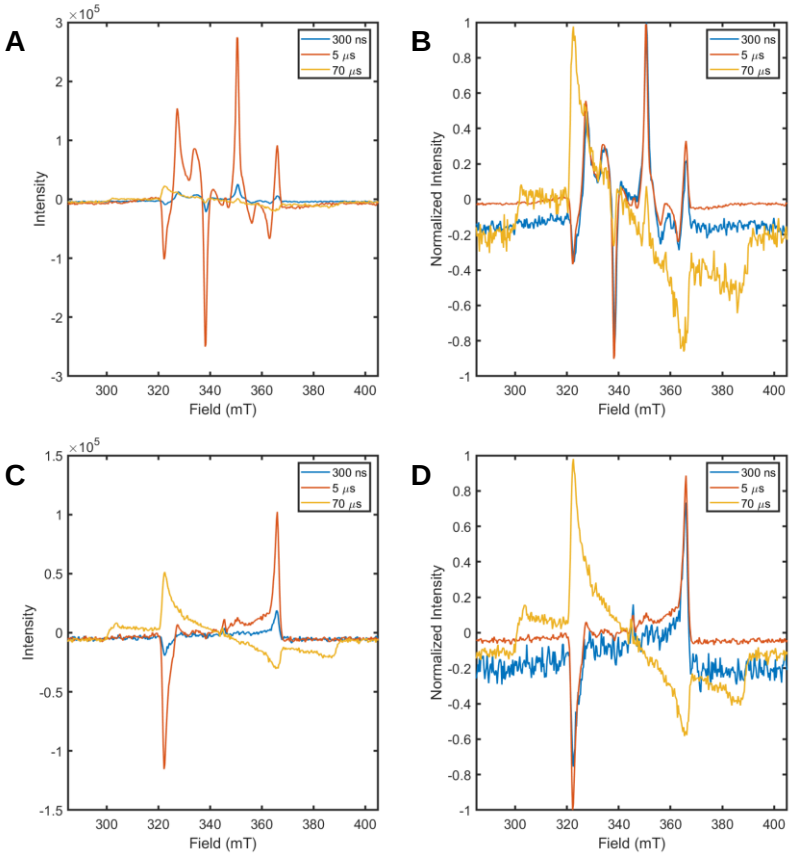

Figure 5.1 EDFS of $Li_2(DPP\text{-}Pent)_2$ at 17 dB microwave power attenuation (quintet-selective) collected at 300 ns, 5 μs, and 70 μs at absolute (**A**) and normalized (**B**) intensity. EDFS at 12 dB microwave power attenuation (triplet-selective) collected at 300 ns, 5 μs, and 70 μs at absolute (**C**) and normalized (**D**) intensity.

The triplet-selective EDFS collected at 12 dB microwave attenuation is dominated by the triplet features. These also rise going from 300 ns to 5 μs before decaying slightly in intensity

toward 70 μs as seen in Figure 5.1C. The polarization pattern of the triplet begins in a *eeaa* pattern where *a* stands for absorptive and *e* for emissive and the four positions correspond to parallel, perpendicular, perpendicular, parallel orientations of the spin packets involved in the two transitions observed in this region. At long DAFs, the polarization pattern changes to *aaee*, suggesting a redistribution of the population density among the magnetic sublevels of the triplet.

The quintet spectrum could be simulated using the triplet pair Hamiltonian above as shown in Figure 5.2. The eigenenergies and states are solved in the uncoupled basis, so the initial population is set to be the ^{1}(TT) projected into the uncoupled basis. This gives rise to quintet features via the off-diagonal elements of the spin Hamiltonian arising from the dipolar interactions. The spectrum was simulated using a g value of 2.0023, D value of 1250 MHz, E value of 10 MHz, and J value of 20 GHz (as per the convention used in EasySpin, the positive exchange coupling constant places the low spin multiplicity states lowest in energy).

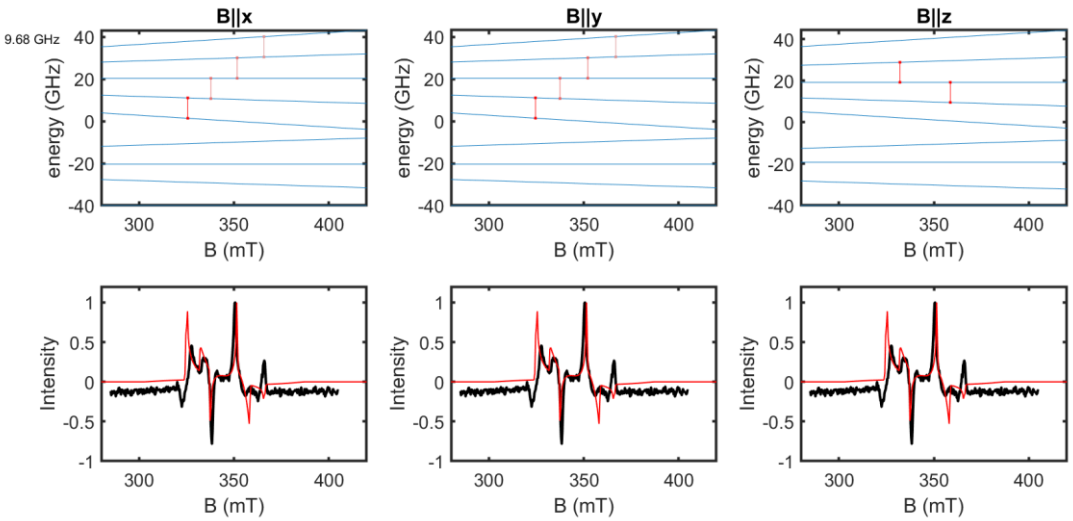

Figure 5.2 Simulated ^{5}(TT) TREPR spectrum (red lines in lower plots) overlaid on the EDFS spectrum of Li_2(DPP-Pent)$_2$ collected at 300 ns DAF and at 20 K, 9.68 GHz microwave frequency.

The levelsplot at each canonical orientation is shown above – the system is largely axial, so the x and y orientations are nearly identical (the rhombicity parameter is not well distinguished from linewidth effects).

The triplet spectrum could be well simulated with the inclusion of the Zeeman and zero-field splitting Hamiltonians in the spin Hamiltonian using a g value of 2.0023, D value of 1250 MHz, and an E value of 10 MHz. The simulated results are overlayed on the triplet spectrum at 5 μs in Figure 5.3.

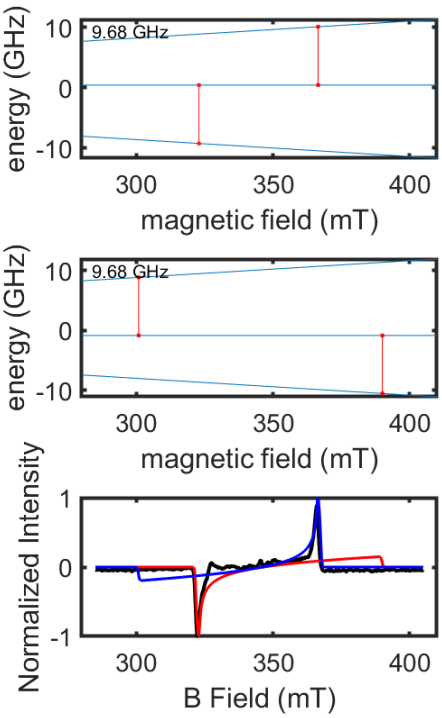

Figure 5.3 Simulated triplet TREPR spectrum (red and blue lines in lower plots) overlaid on the EDFS spectrum of Li_2(DPP-Pent)$_2$ collected at 5 μs DAF and at 20 K, 9.68 GHz microwave frequency. The top levelsplot shows the perpendicular orientations (x and y) and the middle levelsplot shows the parallel orientations (z) of the spin system with respect to the magnetic field.

The time traces of the quintet features at 338.0 and 350.4 mT are shown in Figure 5.4. These traces could be fit with a biexponential function which is shown overlaid over the data in Figure 6.4C. At 338.0 mT, we obtain time constants τ_1 = 1.84 μs and τ_2 = 19.4 μs reflecting the rise and decay times of the signal, respectively. At 350.4 mT, we obtain time constants τ_1 = 1.43 μs and τ_2 = 19.3 μs reflecting the rise and decay times of the signal, respectively.

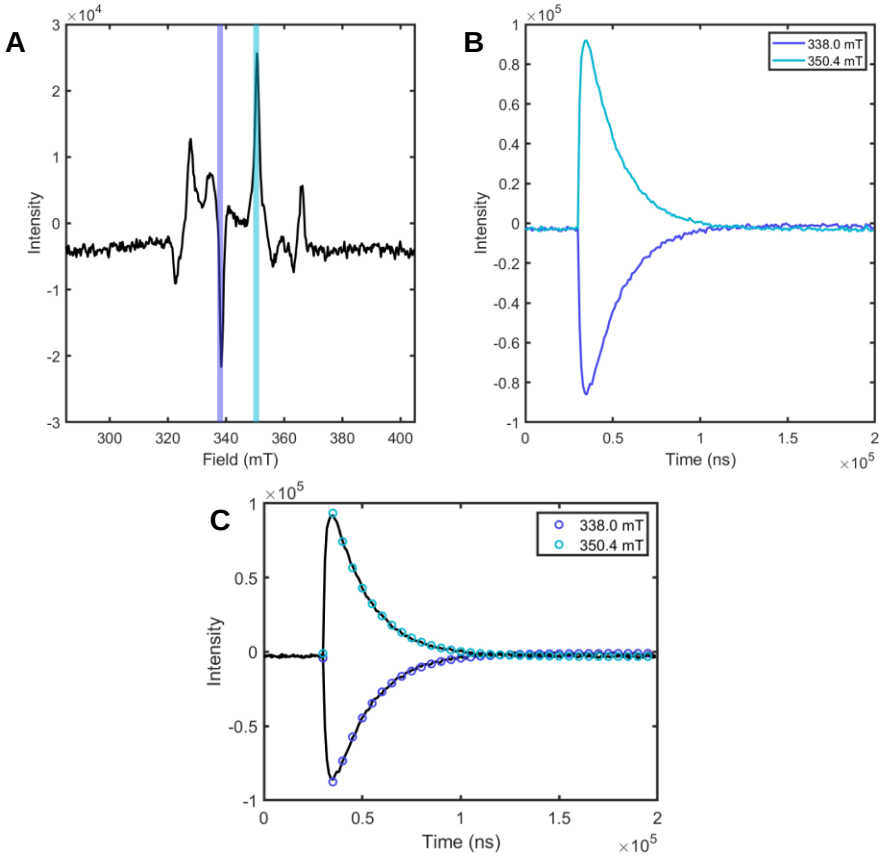

Figure 5.4 (**A**) Quintet spectrum at 5 μs of Li_2(DPP-Pent)$_2$ with field positions 338.0 mT and 350.4 mT highlighted. (**B**) The kinetic traces of the amplitude observed at 338.0 and 350.4 mT in purple and teal, respectively, where the time axis represents the DAF time. (**C**) The time traces overlaid with the results of a biexponential fit.

As previously mentioned, the polarization pattern of the triplet features changes over the times observed. This is shown more explicitly in the time traces collected at 322.2 and 366.0 mT in Figure 5.5.

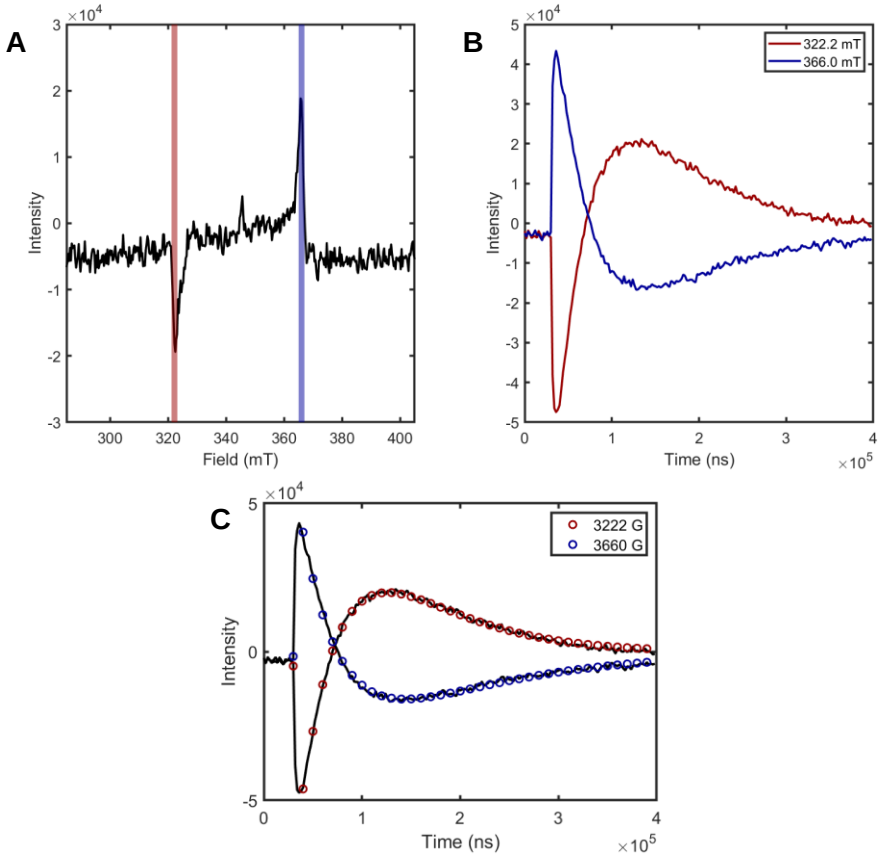

Figure 5.5 (**A**) Triplet spectrum at 300 ns of $Li_2(DPP\text{-}Pent)_2$ with field positions 322.2 and 366.0 mT highlighted. (**B**) The kinetic traces of the amplitude observed at 322.2 and 366.0 mT in red and blue, respectively, where the time axis represents the DAF time. (**C**) The time traces overlaid with the results of a triexponential fit.

The kinetic traces could be fit with a triexponential function, yielding time constants at 322.2 mT of τ_1 = 2.87 μs, τ_2 = 52.49 μs, τ_3 = 60.73 μs and time constants at 366.0 mT of τ_1 = 2.224 μs, τ_2 = 40.52 μs, τ_3 = 131.2 μs. The change in polarization pattern has been observed in correlated

radical pairs as well and arises due to spin-selective intersystem crossing back to the ground state from the triplet sublevels.[9]

A radical standard was added to the sample containing Li_2(DPP-Pent)$_2$ and used to reference the phasing of the data – the radical, which is not affected by the laser flash and exhibits Boltzmann population of its magnetic sublevels, should exhibit a net absorptive feature around the free electron g value ~2.0023. The radical also acts as a reference for Rabi nutation experiments at fixed microwave drive power and varied field position. Observing the ratio of the obtained nutation frequencies can corroborate the assignment of transitions within the S = 1 and S = 2 manifolds.

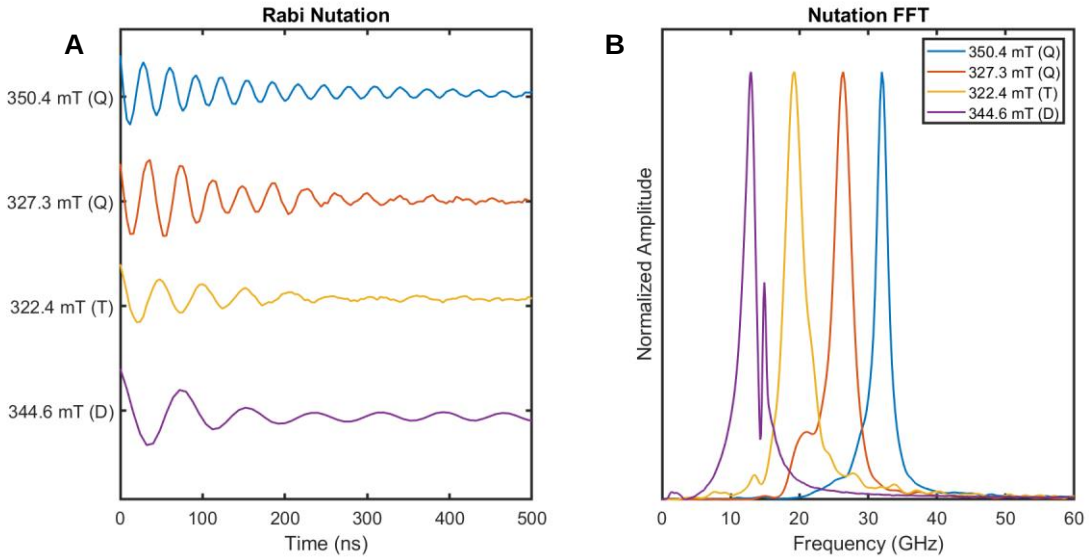

Figure 5.6 Rabi nutation experiments collected on the Li_2(DPP-Pent)$_2$ sample with added reference radical species at 14 dB microwave attenuation at 20 K observed at 350.4 mT (Quintet ~M_s = 0 ↔ +1, perpendicular, 5 μs DAF), 327.3 mT (Quintet ~M_s = -2 ↔ -1, perpendicular, 5 μs

DAF), 322.4 mT (Triplet ~ M_s = -1 ↔ 0, perpendicular, 90 μs DAF), and 344.6 mT (Doublet ~ M_s = -1/2 ↔ +1/2, 90 μs DAF).

As shown in Figure 5.6, Rabi nutation experiments were collected at 350.4, 327.3, 322.4, and 344.6 mT which correspond to quintet (~M_s = 0 ↔ +1, perpendicular), quintet (~M_s = -2 ↔ -1, perpendicular), triplet (~M_s = -1 ↔ 0, perpendicular), and the stable radical (M_s = -1/2 ↔ +1/2) transitions, respectively. The fast Fourier transform of the data provides nutation frequencies of 32.2 GHz (at 350.4 mT), 26.6 GHz (at 327.3 mT), 19.5 GHz (at 322.4 mT), and 13.1 GHz (at 344.6 mT). We can determine the expected ratios of the Rabi nutation frequencies for each given transition from Eq. 6.1. We expect $\frac{\Omega_{Q(0\leftrightarrow+1)}}{\Omega_{Q(-2\leftrightarrow-1)}} = \sqrt{\frac{3}{2}} \approx 1.22, \frac{\Omega_{Q(0\leftrightarrow+1)}}{\Omega_{T(-1\leftrightarrow0)}} = \sqrt{3} \approx 1.73, \frac{\Omega_{Q(0\leftrightarrow+1)}}{\Omega_{D(-1/2\leftrightarrow+1/2)}} = \sqrt{6} \approx 2.45$. Taking the ratio of the experimentally derived nutation frequencies we get $\frac{\Omega_{Q(0\leftrightarrow+1)}}{\Omega_{Q(-2\leftrightarrow-1)}} = 1.21$, $\frac{\Omega_{Q(0\leftrightarrow+1)}}{\Omega_{T(-1\leftrightarrow0)}} = 1.65$, and $\frac{\Omega_{Q(0\leftrightarrow+1)}}{\Omega_{D(-1/2\leftrightarrow+1/2)}} = 2.47$, which is consistent with our expectations.

HDPP-Pent

TREPR was collected on 2 mM glassed solutions of HDPP-Pent. The EDFS collected at 17 dB are shown in Figures 6.7A and 6.7B from 5 to 70 μs. The contribution of the triplet features is significantly reduced compared to the data acquired on Li_2(DPP-Pent)$_2$. In fact, the EDFS collected at 12 dB, which should be dominated by pure triplet features, is largely noise as shown in Figures 6.7C and 6.7D. This as well stands in stark contrast to the evident triplet features that dominate the EDFS at this drive power in Li_2(DPP-Pent)$_2$. There is a small radical impurity observed in the EDFS centered at 345.2 mT.

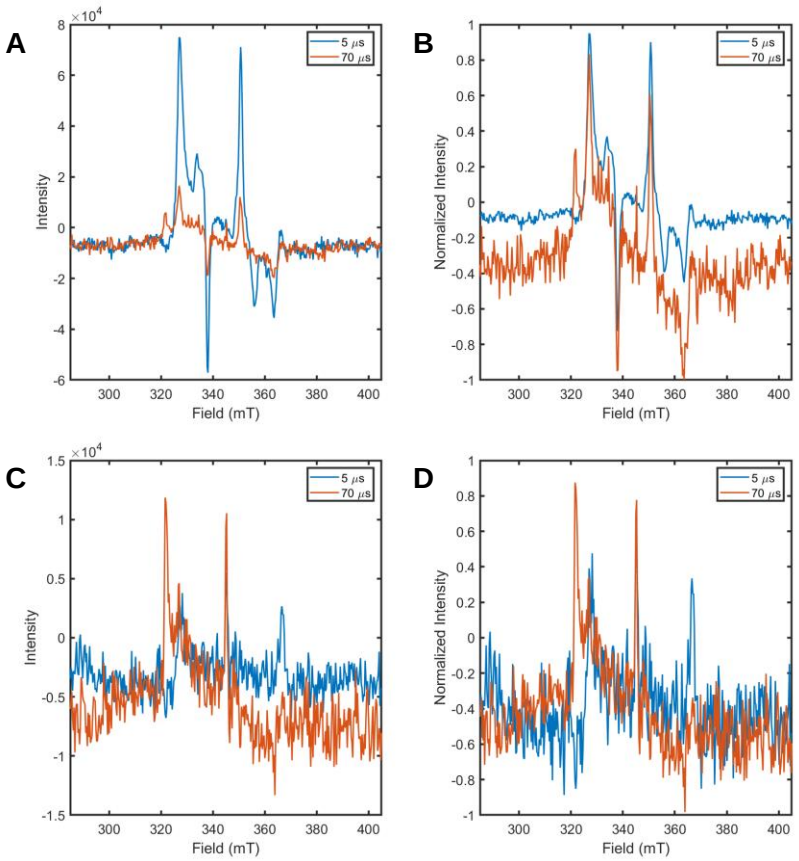

Figure 5.7 EDFS of HDPP-Pent at 17 dB microwave power attenuation (quintet-selective) collected at 5 and 70 μs at absolute (**A**) and normalized (**B**) intensity. EDFS at 12 dB microwave power attenuation (triplet-selective) collected at 5 and 70 μs at absolute (**C**) and normalized (**D**) intensity.

The quintet features from the EDFS of HDPP-Pent could be simulated with our spin Hamiltonian. The spectrum was reasonably simulated using a g value of 2.0023, D value of 1050 MHz, E value of 10 MHz, and J value of 20 GHz. The simulations are overlaid on the data in Figure 5.8 with accompanying levelsplots at perpendicular (only x-direction shown) and parallel (z) orientations.

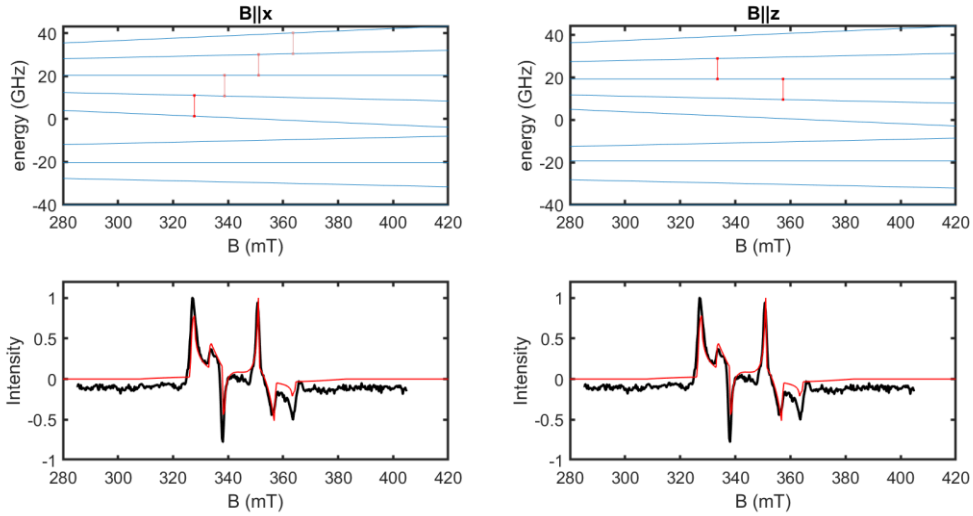

Figure 5.8 Simulated ^{5}(TT) TREPR spectrum (red lines in lower plots) overlaid on the EDFS spectrum of HDPP-Pent collected at 5 μs DAF and at 20 K, 9.68 GHz microwave frequency. The levelsplot at each perpendicular (x) and parallel (z) orientations are shown above.

The kinetic traces acquired on the quintet spectrum are shown in Figure 5.9. Following the kinetics at 338.0 and 350.8 mT, which correspond to ~M_s = -1 ↔0 and ~M_s = 0 ↔ +1 transitions, respectively, we can fit the evolution of these features to a biexponential. At 338.0 mT, we obtain time constants of τ_1 = 7.28 μs and τ_2 = 32.5 μs corresponding to rise and decay of the signal, respectively. At 350.8 mT, we obtain time constants of τ_1 = 5.15 μs and τ_2 = 37.1 μs corresponding to rise and decay of the signal, respectively. These fits are overlaid on the kinetic traces in Figure 5.9C.

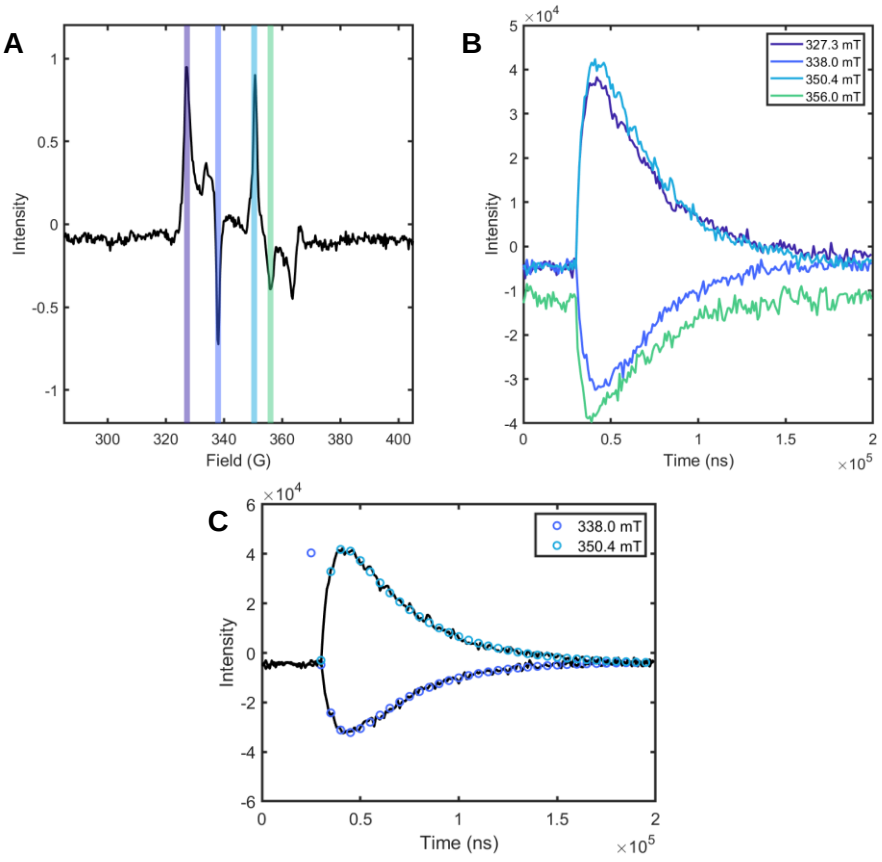

Figure 5.9 (**A**) Quintet spectrum at 5 μs of HDPP-Pent with field positions 338.0 mT and 350.8 mT highlighted. (**B**) The kinetic traces of the amplitude observed at 338.0 and 350.8 mT in purple and light blue, respectively, where the time axis represents the DAF time. (**C**) The time traces overlaid with the results of a biexponential fit.

Rabi nutation experiments were carried out at 5 μs DAF at field positions 350.4, 327.3, and 345.2 mT, which correspond to quintet ~$M_s = 0 \leftrightarrow +1$ transitions at perpendicular orientations, quintet ~$M_s = -2 \leftrightarrow -1$ transitions at perpendicular orientations, and radical impurity $M_s = -1/2 \leftrightarrow +1/2$ transitions. The data is summarized in Figure 5.10. The ratio of the nutation frequencies are

$\frac{\Omega_{Q(0\leftrightarrow+1)}}{\Omega_{Q(-2\leftrightarrow-1)}} = 1.21$ and $\frac{\Omega_{Q(0\leftrightarrow+1)}}{\Omega_{D(-1/2\leftrightarrow+1/2)}} = 2.56$, which is consistent with the expected values of $\sqrt{\frac{3}{2}} \approx 1.22$ and $\sqrt{6} \approx 2.45$.

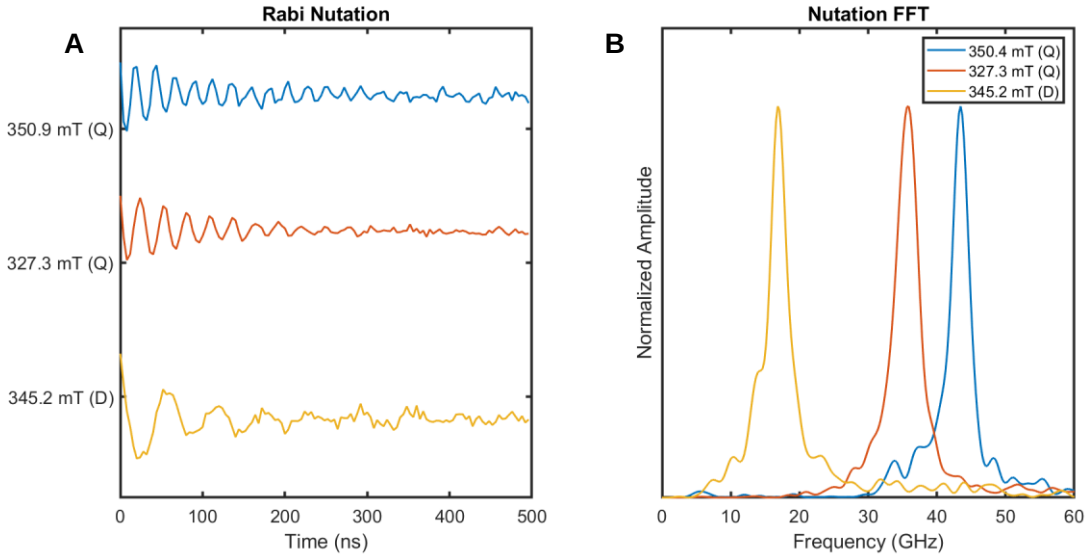

Figure 5.10 Rabi nutation experiments collected on the HDPP-Pent sample at 14 dB microwave attenuation at 20 K observed at 350.8 mT (Quintet ~$M_s = 0 \leftrightarrow +1$, perpendicular, 5 μs DAF), 327.3 mT (Quintet ~$M_s = -2 \leftrightarrow -1$, perpendicular, 5 μs DAF), and 354.2 mT (Doublet impurity ~ $M_s = -1/2 \leftrightarrow +1/2$, 5 μs DAF).

KDPP-Pent

TREPR was collected on 2 mM glassed solutions of KDPP-Pent. The EDFS collected at 20 dB are shown in Figures 5.11A and 5.11B from 5 to 100 μs. The contribution of the triplet features is substantial at this power attenuation. The triplet optimized EDFS collected at 14 dB are shown in shown in Figures 5.11C and 5.11D. The triplet spectrum, even at early times, demonstrates the opposite polarization pattern than that observed for Li_2(DPP-Pent)$_2$ at early times

and is rather similar to the long-time triplet spectra observed for Li_2(DPP-Pent)$_2$. The polarization pattern is similar to that observed for intersystem crossing-populated triplets.

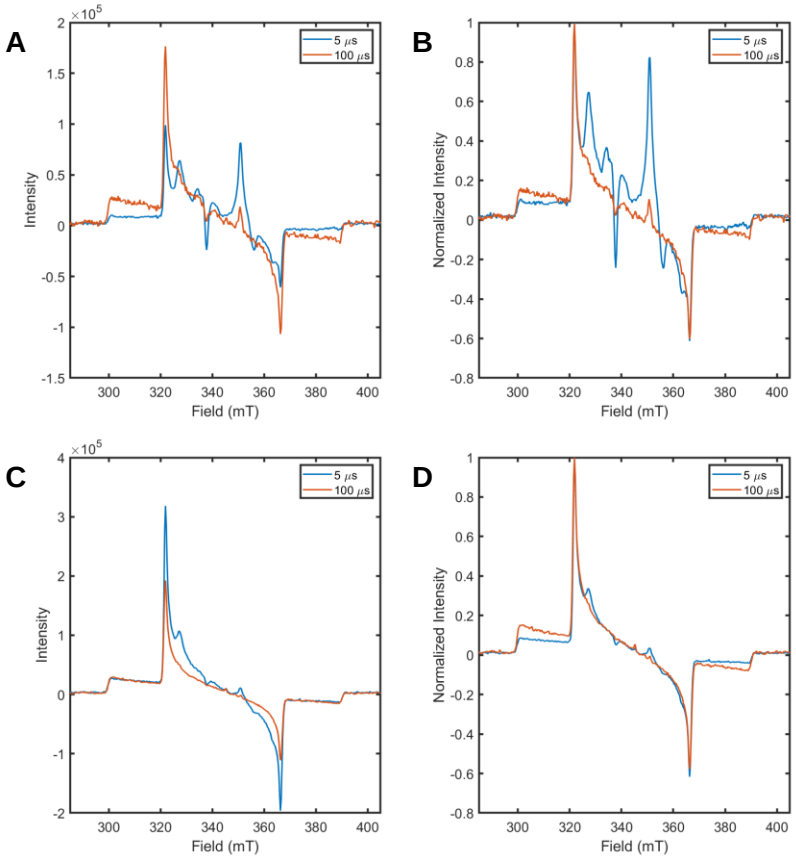

Figure 5.11 EDFS of KDPP-Pent at 20 dB microwave power attenuation (quintet-selective) collected at 5 and 100 μs at absolute (**A**) and normalized (**B**) intensity. EDFS at 14 dB microwave power attenuation (triplet-selective) collected at 5 and 100 μs at absolute (**C**) and normalized (**D**) intensity.

The quintet features from the EDFS of KDPP-Pent could be reasonably simulated using a g value of 2.0023, D value of 1050 MHz, E value of 10 MHz, and J value of 20 GHz. The simulations are overlaid on the data in Figure 5.12 with accompanying levelsplots at perpendicular (only x-direction shown) and parallel (z) orientations.

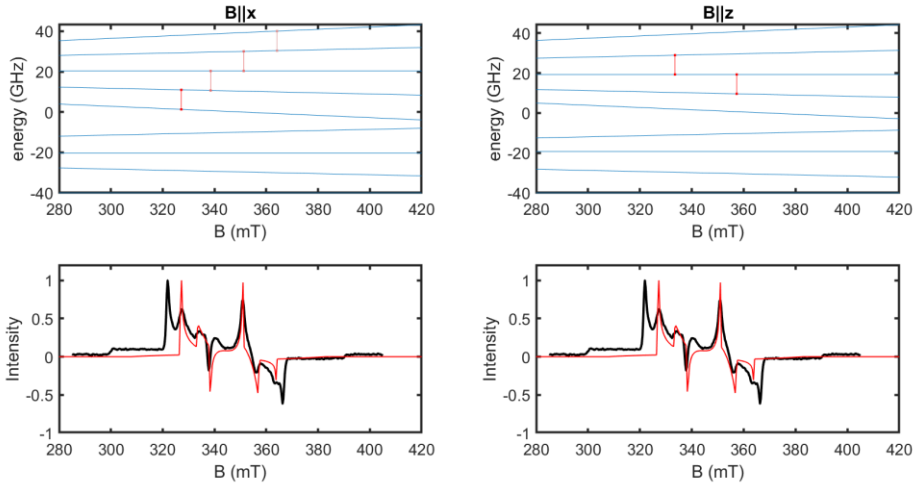

Figure 5.12 Simulated ^{5}(TT) TREPR spectrum (red lines in lower plots) overlaid on the EDFS spectrum of KDPP-Pent collected at 5 μs DAF and at 20 K, 9.68 GHz microwave frequency. The levelsplot at each perpendicular (x) and parallel (z) orientations re shown above.

The kinetic traces acquired at 327.3, 337.8, 350.9, and 356.0 mT are shown in Figure 5.13B. We fit the traces at 337.8 and 350.9 mT to a biexponential function. At 337.8 mT, we obtain time constants of τ_1 = 9.82 μs and τ_2 = 26.3 μs corresponding to rise and decay of the signal, respectively. At 350.9 mT, we obtain time constants of τ_1 = 3.93 μs and τ_2 = 31.0 μs corresponding to rise and decay of the signal, respectively. These fits are overlaid on the kinetic traces in Figure 5.13C.

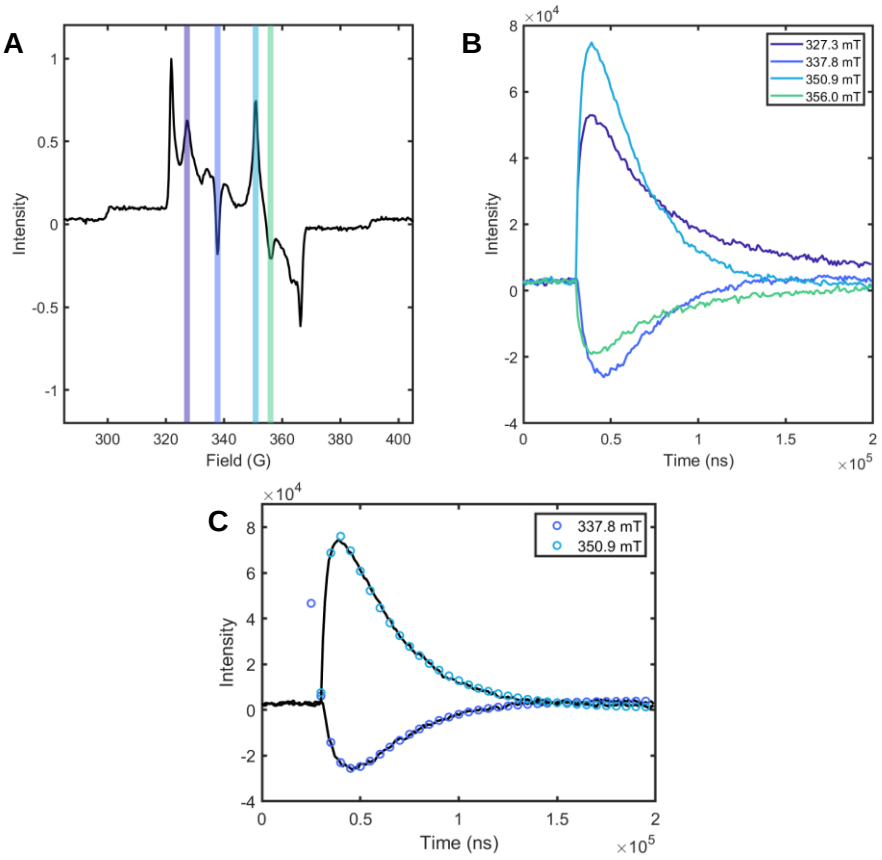

Figure 5.13 (**A**) Quintet spectrum at 5 μs of KDPP-Pent with field positions 337.8 mT and 350.9 mT highlighted. (**B**) The kinetic traces of the amplitude observed at 337.8 and 350.9 mT in purple and light blue, respectively, where the time axis represents the DAF time. (**C**) The time traces overlaid with the results of a biexponential fit.

The kinetic traces of the triplet optimized TREPR spectrum of KDPP-Pent at 321.9 and 366.0 mT, corresponding to the perpendicular extrema of the -1 ↔ 0 and 0 ↔ +1 transitions respectively, are shown in Figure 5.14. Notably, the triplet features appear within the instrument response time. This is unlike $Li_2(DPP\text{-}Pent)_2$ where they grow in roughly on the same timescale as the quintet features (several microseconds).

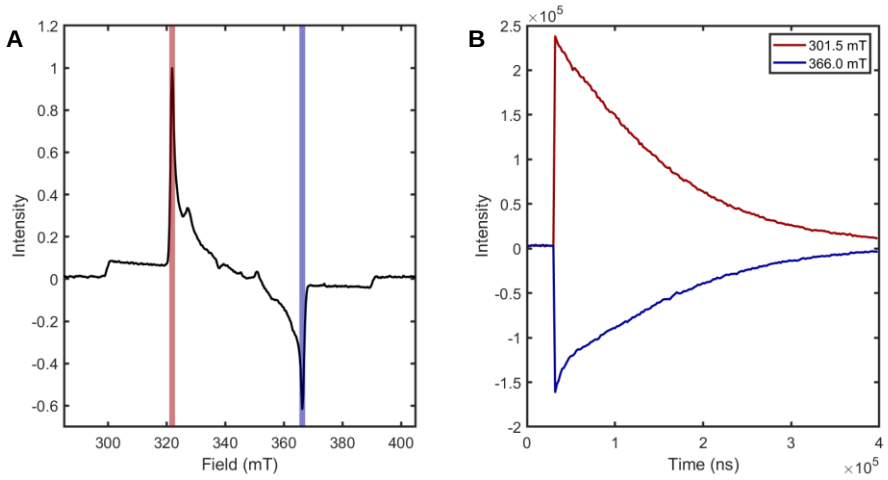

Figure 5.14 (**A**) The triplet optimized TREPR spectrum of KDPP-Pent at 5 μs DAF, 14 dB attenuation with 321.9 and 366.0 mT highlighted in red and blue, respectively. (**B**) The kinetic traces collected at 321.9 and 366.0 mT.

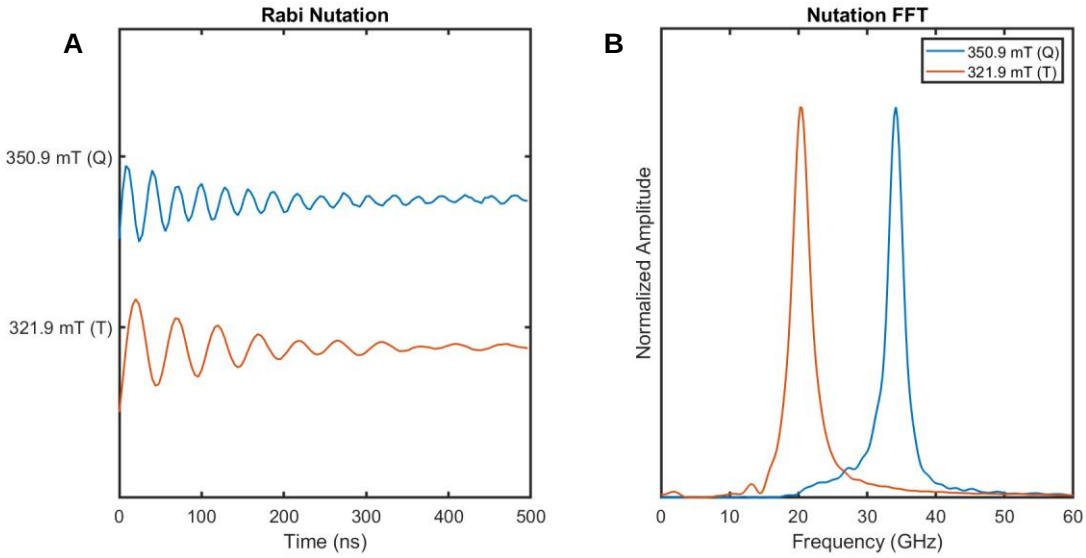

Figure 5.15 Rabi nutation experiments collected on the KDPP-Pent sample at 14 dB microwave attenuation at 20 K observed at 350.8 mT (Quintet ~$M_s = 0 \leftrightarrow +1$, perpendicular, 5 μs DAF) and 321.9 mT (Triplet ~$M_s = -1 \leftrightarrow 0$, perpendicular, 5 μs DAF).

Rabi nutation experiments were carried out at 350.9 mT (quintet, ~M_s = 0 ↔ +1, perpendicular) and 321.9 mT (triplet, ~M_s = -1 ↔ 0) and are shown in Figure 5.15. The nutation frequencies obtained from fast Fourier transform were 34.4 GHz (350.9 mT) and 20.5 GHz (321.9 mT). The ratio of these two gives $\frac{\Omega_{Q(0\leftrightarrow+1)}}{\Omega_{T(-1\leftrightarrow0)}} = 1.68$ which is consistent with the expected ratio of $\sqrt{3} \approx 1.73$ and corroborates our assignment of these features.

Discussion and Summary

In summary, we have examined the TREPR data for Li_2(DPP-Pent)$_2$, HDPP-Pent, and KDPP-Pent. Discussion in the literature has suggested that the quintet states may play a role in the dephasing of the triplet pair state, giving rise to free triplets. Alternatively, they may help ultimately populate overall S = 1 pair states that can undergo triplet-triplet annihilation to provide a sole triplet state. Li_2(DPP-Pent)$_2$ exhibits a dataset most in line with expectations from other TREPR studies on singlet fission systems wherein the quintet and triplet features rise within the microsecond timescale. HDPP-Pent, however, features no substantial signal arising from free triplets in the timescales observed here. KDPP-Pent as well strays from the pack by exhibiting strong triplet features that rise within the instrument response, preceding the rise of the quintet features. KDPP-Pent also exhibits a polarization pattern that is most consistent with a triplet populated by intersystem crossing, or the polarization pattern observed in the triplet spectra at long DAFs in Li_2(DPP-Pent)$_2$. The investigation into the origin of these differences between the DPP-Pent series is ongoing.

Citations

(1) Smith, M. B.; Michl, J. Singlet Fission. *Chem. Rev.* **2010**, *110* (11), 6891–6936. https://doi.org/10.1021/cr1002613.

(2) Merrifield, R. E. Magnetic Effects on Triplet Exciton Interactions. *Pure and Applied Chemistry* **1971**, *27* (3), 481–498. https://doi.org/10.1351/pac197127030481.
(3) Benk, H.; Sixl, H. Theory of Two Coupled Triplet States. *Molecular Physics* **1981**, *42* (4), 779–801. https://doi.org/10.1080/00268978100100631.
(4) Piland, G. B.; Burdett, J. J.; Dillon, R. J.; Bardeen, C. J. Singlet Fission: From Coherences to Kinetics. *J. Phys. Chem. Lett.* **2014**, *5* (13), 2312–2319. https://doi.org/10.1021/jz500676c.
(5) Weiss, L. R.; Bayliss, S. L.; Kraffert, F.; Thorley, K. J.; Anthony, J. E.; Bittl, R.; Friend, R. H.; Rao, A.; Greenham, N. C.; Behrends, J. Strongly Exchange-Coupled Triplet Pairs in an Organic Semiconductor. *Nature Phys* **2017**, *13* (2), 176–181. https://doi.org/10.1038/nphys3908.
(6) Tayebjee, M. J. Y.; Sanders, S. N.; Kumarasamy, E.; Campos, L. M.; Sfeir, M. Y.; McCamey, D. R. Quintet Multiexciton Dynamics in Singlet Fission. *Nature Phys* **2017**, *13* (2), 182–188. https://doi.org/10.1038/nphys3909.
(7) Basel, B. S.; Zirzlmeier, J.; Hetzer, C.; Reddy, S. R.; Phelan, B. T.; Krzyaniak, M. D.; Volland, M. K.; Coto, P. B.; Young, R. M.; Clark, T.; Thoss, M.; Tykwinski, R. R.; Wasielewski, M. R.; Guldi, D. M. Evidence for Charge-Transfer Mediation in the Primary Events of Singlet Fission in a Weakly Coupled Pentacene Dimer. *Chem* **2018**, *4* (5), 1092–1111. https://doi.org/10.1016/j.chempr.2018.04.006.
(8) Lubert-Perquel, D.; Salvadori, E.; Dyson, M.; Stavrinou, P. N.; Montis, R.; Nagashima, H.; Kobori, Y.; Heutz, S.; Kay, C. W. M. Identifying Triplet Pathways in Dilute Pentacene Films. *Nat Commun* **2018**, *9* (1), 4222. https://doi.org/10.1038/s41467-018-06330-x.
(9) Bayliss, S. L.; Weiss, L. R.; Kraffert, F.; Granger, D. B.; Anthony, J. E.; Behrends, J.; Bittl, R. Probing the Wave Function and Dynamics of the Quintet Multiexciton State with Coherent Control in a Singlet Fission Material. *Phys. Rev. X* **2020**, *10* (2), 021070. https://doi.org/10.1103/PhysRevX.10.021070.
(10) Chen, M.; Krzyaniak, M. D.; Nelson, J. N.; Bae, Y. J.; Harvey, S. M.; Schaller, R. D.; Young, R. M.; Wasielewski, M. R. Quintet-Triplet Mixing Determines the Fate of the Multiexciton State Produced by Singlet Fission in a Terrylenediimide Dimer at Room Temperature. *Proceedings of the National Academy of Sciences* **2019**, *116* (17), 8178–8183. https://doi.org/10.1073/pnas.1820932116.
(11) Bayliss, S. L.; Weiss, L. R.; Mitioglu, A.; Galkowski, K.; Yang, Z.; Yunusova, K.; Surrente, A.; Thorley, K. J.; Behrends, J.; Bittl, R.; Anthony, J. E.; Rao, A.; Friend, R. H.; Plochocka, P.; Christianen, P. C. M.; Greenham, N. C.; Chepelianskii, A. D. Site-Selective Measurement of Coupled Spin Pairs in an Organic Semiconductor. *Proceedings of the National Academy of Sciences* **2018**, *115* (20), 5077–5082. https://doi.org/10.1073/pnas.1718868115.
(12) Nagashima, H.; Kawaoka, S.; Akimoto, S.; Tachikawa, T.; Matsui, Y.; Ikeda, H.; Kobori, Y. Singlet-Fission-Born Quintet State: Sublevel Selections and Trapping by Multiexciton Thermodynamics. *J. Phys. Chem. Lett.* **2018**, *9* (19), 5855–5861. https://doi.org/10.1021/acs.jpclett.8b02396.
(13) Basel, B. S.; Zirzlmeier, J.; Hetzer, C.; Phelan, B. T.; Krzyaniak, M. D.; Reddy, S. R.; Coto, P. B.; Horwitz, N. E.; Young, R. M.; White, F. J.; Hampel, F.; Clark, T.; Thoss, M.; Tykwinski, R. R.; Wasielewski, M. R.; Guldi, D. M. Unified Model for Singlet Fission within a Non-Conjugated Covalent Pentacene Dimer. *Nat Commun* **2017**, *8* (1), 15171. https://doi.org/10.1038/ncomms15171.

(14) Smyser, K. E.; Eaves, J. D. Singlet Fission for Quantum Information and Quantum Computing: The Parallel JDE Model. *Sci Rep* **2020**, *10* (1), 18480. https://doi.org/10.1038/s41598-020-75459-x.
(15) Lewis, S. G.; Smyser, K. E.; Eaves, J. D. Clock Transitions Guard against Spin Decoherence in Singlet Fission. *J. Chem. Phys.* **2021**, *155* (19), 194109. https://doi.org/10.1063/5.0069344.
(16) Stoll, S.; Jeschke, G.; Willer, M.; Schweiger, A. Nutation-Frequency Correlated EPR Spectroscopy: The PEANUT Experiment. *Journal of Magnetic Resonance* **1998**, *130* (1), 86–96. https://doi.org/10.1006/jmre.1997.1285.
(17) Collins, M. I.; McCamey, D. R.; Tayebjee, M. J. Y. Fluctuating Exchange Interactions Enable Quintet Multiexciton Formation in Singlet Fission. *J. Chem. Phys.* **2019**, *151* (16), 164104. https://doi.org/10.1063/1.5115816.
(18) Bencini, A.; Gatteschi, D. *EPR of Exchange Coupled Systems*; Courier Corporation, 2012.
(19) Weil, J. A.; Bolton, J. R. Basic Principles of Paramagnetic Resonance. In *Electron Paramagnetic Resonance*; John Wiley & Sons, Ltd, 2006; pp 1–35. https://doi.org/10.1002/9780470084984.ch1.
(20) McWeeny, R. *Spins in Chemistry*; Dover Publications, 2004.
(21) Yunusova, K. M.; Bayliss, S. L.; Chanelière, T.; Derkach, V.; Anthony, J. E.; Chepelianskii, A. D.; Weiss, L. R. Spin Fine Structure Reveals Biexciton Geometry in an Organic Semiconductor. *Phys. Rev. Lett.* **2020**, *125* (9), 097402. https://doi.org/10.1103/PhysRevLett.125.097402.
(22) Stoll, S.; Schweiger, A. EasySpin, a Comprehensive Software Package for Spectral Simulation and Analysis in EPR. *Journal of Magnetic Resonance* **2006**, *178* (1), 42–55. https://doi.org/10.1016/j.jmr.2005.08.013.